16

Computations of Flowfield over Reentry Modules at High Speed

R. C. Mehta[1,2]
[1]*Noorul Islam University, Kumaracoil,*
[2]*Formally, Nanyang Technological University*
[1]*India*
[2]*Singapore*

1. Introduction

A high-speed flow-past a reentry capsule generates a bow shock wave which causes a rather high surface pressure and as a result the development of high aerodynamic drag which is require for aero-braking purposes. Highly blunt configurations are generally preferred to decelerate space-capsule for safe returning on the Earth after performing the experiments. The bow shock wave is detached from the blunt fore-body and is having a mixed subsonic-supersonic region between them. The wall pressure distribution, the location of the sonic line and shock stand-off distance on the spherical cap region have been analytically calculated at very high speeds with an adiabatic index near to unity which gives a singular point at 60 deg from the stagnation point (Chester, 1956; Freeman 1956). The analytical approach for the high-speed flow over the blunt-body is considerably difficult and complex (Lighthill 1957). The flow-field over the reentry capsule becomes further complicated due to the presence of corner at the shoulder and the base shell of the reentry module.
Reentry capsule configurations significantly differ from each other due to entry conditions, trajectory, and a number of aerodynamic factors such as aerodynamic axial force, normal force, static moment, damping coefficients. This leads to the necessity to investigate the influence of the shape of blunted bodied on the flow field and aerodynamic characteristics. (Bedin et al., 1992) have presented aerodynamic characteristics and geometrical parameters for the sixteen different reentry modules using experimental data of ballistic test facility. Aero-assist flight experiment (AFE) configurations have been analyzed using two different Navier-Stokes flow solvers by (Venkatapathy et al., 1991). Aerodynamic heating and pressure along with the fore-body and wake-flow structure during atmospheric entry of the Mars Pathfinder spacecraft have been computed by (Hass & Venkatapathy, 1995) using the commercially available general atmospheric simulation program (GASP 2.2). An aerodynamic analysis of the commercial experiment transport (COMET) reentry capsule has been carried out by (Wood et al., 1996) solving the laminar thin layer Navier-Stokes LAURA code for low supersonic to hypersonic speeds. The LAURA code is an upwind, point implicit, second-order accurate fluid dynamics solver based on an extension of the Roe flux-difference splitting scheme. (Yamomoto & Yoshioka, 1995) carried out flow field computation over the OREX (orbital reentry experiments) using computational fluid dynamics approach coupled with the thermal response of the heat shield material using

finite element method in conjunction with the aerodynamic flight data. (Tam, 1992) has computed flow field at hypersonic Mach numbers over Viking, Biconic and AFE reentry capsules employing IEC3D (Inviscid Equilibrium Computation in 3-Dimension). (Menne, 1994) has computed flow field over Viking similar to the Apollo type module and Biconic configurations for freestream Mach numbers 2.0 and 3.0 by solving compressible Euler equations. The inviscid analysis is unable to show the flow separation in the back shell region of the reentry capsule. The aerodynamic characterization of the CARINA reentry module in the low supersonic Mach regimes has been performed employing numerical and experimental methods (Solazzo et al., 1994). The flow field simulation over the ARD (ESA's atmospheric reentry demonstrator) module has been computed numerically by (Walpot, 2001) at hypersonic speeds. Developments relating to the base pressure and the base heating prediction for wide range of cone and wedge have been reviewed for supersonic and hypersonic Mach numbers by (Lamb & Oberkampf, 1995). The flow field simulations over the Beagle-2 spacecraft have been carried out by (Liever et al., 2003) using CFD-FASTRAN code for low supersonic to hypersonic speeds. A numerical simulation code has been applied for super orbital reentry flow and has been used to the flow field prediction around the MUSES-C reentry module (Osu et al., 2002). Supersonic and hypersonic flow past a slender cone (Tai & Kao, 1994) has been numerically simulated by solving Navier-Strokes using an explicit multi-stage Roe's method. The flow fields around blunt reentry modules (Teramoto et al., 2001) were numerically analyzed in order to investigate the mechanism of dynamic instability of the capsule at freestream Mach number of 1.3. The blunt and short reentry capsule tends to be dynamically unstable at low supersonic Mach number attributed primarily to the delay in base pressure (Teramoto & Fujii, 2001). Numerical studies have been done by (Ottens, 2001) employing a laminar Navier-stokes flow solver for two different types of Delft aerospace reentry test (DART) demonstrators reentry capsules.

The frontal shape of the reentry body can be classified either employing as a spherical cap as in the case of the Apollo and the ARD, or combination of the spherical nose or blunted-body with cone as in the case of the OREX and the Beagle-2, or a spherical blunt-cone/flare configuration as proposed by DART. The flow field features over the reentry capsule can be delineated through the experimental and numerical flow simulations (Mehta, 2006) at high speeds. Figure 1 shows schematic flow field features over the OREX and the DART capsules. The significant flow features are described by the following. In the fore-body region, the fluid decelerates through the bow shock wave depending on the cruise speed and altitude. As the shoulder of the capsule, the flow turns and expands rapidly and boundary layer detached, forming a free shear layer that separates the inner re-circulating flow region behind the base from the outer flow field. The latter is recompressed and turned back to the freestream direction, first by the so-called lip shock, and further downstream by recompression shock. At the end of the re-circulating flow past the neck, the shear layer develops in the wake trail. A complex inviscid wave structure often includes a lip shock wave (associates with the corner expansion) and wake trail (adjacent to the shear layer confluence). The corner expansion process is a modified Prandtl-Meyer patter distorted by the presence of the approaching boundary layer. An excellent review of the thermodynamic and chemical-kinetic models used for computational fluid dynamics simulations of a non-equilibrium flow field is reported by (Gnoffo & Pettnelli, 1995). Another review of the after body aero-thermal flight data and thermal protection system design for Mercury, Gemini, Project Fire, Apollo, Reentry F, Mars Viking, Galileo, Mars Pathfinder, MIRKA, Atmospheric Reentry Demonstrator (ARD) is given by (Wright et al., 2006). The flight data analysis of the various reentry capsules will be very useful for the numerical simulation purposes.

Aerodynamic performance of Commercial Experiment Transport (COMET) reentry capsule (Allen & Cheng, 1970) is carried out using both the Euler and the laminar thin-layer Navier-Stokes solver LAURA code based on upwind point implicit, and Roe flux difference splitting scheme for supersonic speed range. The small shoulder radius causes a strong compression and acceleration of the flow around the edge of the heat shield, thinning the boundary layer producing locally high heating on the shoulder. (Weinbaum, 1966, & Wood et al. 1996) have analyzed the wake flow field of the capsules.

The conservatism of the after body thermal protection system (TPS) heat shield design of the reentry module will shift the centre of gravity, which reduces the static stability. Wind tunnel test data are usually having the sting interference effects; however shock tunnel having short duration of testing time and free flight (ballistic range) data exist. In the free flight experiments, a scaled model is shot inside a range and orthogonal shadowgraphs are taken as the capsule flies by each shadow graph station. There is no sting in the free flight test. The base flow features observed from the shadow graphs show several known wake features such as shear layers, neck region and recompression shocks. The reentry capsule is usually having a high drag shape with good static stability margin, a simple generic shape to take maximum advantage of available aerodynamic data, nose radius selection for minimum structural mass with maximum drag, leading to a maximum radius limited by the range of bluntness ratios, corner radii minimized for maximum drag, but constrained by structural/ thermal requirements. Figure 2 shows the geometrical details of the various reentry capsules (Mehta, 2006). The large nose radius produces large drag, and the short body length reduces the total weight, resulting in a small ballistic coefficient. To ensure the deployment of the parachute in the transonic region, the attitude of the capsule must be maintained within the limit in the whole speed range. Most of the basic configuration parameters such as nose radii or body lengths are decided mainly from the thermal protection requirement. The centre of gravity of the capsule is located in-forward of the centre of pressure, to get statically stable. (Hiraki et al., 1998) measured the unsteady surface pressure of the oscillating MUSES-C reentry capsule and found that the base pressure is responsible for the dynamic instability. One oscillation cycle corresponds to approximately 150 in non-dimensional time. The dynamic instability occurs at very low reduced frequencies by numerical simulation (Teramoto et al. 2001, & Toramoto & Fujii, 2000) of thin layer RANS using lower-upper alternating direction implicit factorization implicit algorithm in conjunction with higher order by the MUSCL interpolation of primitive variables. Unsteady flow is carried out employing multistage time stepping method (Mehta, 2006).

Table 1(a) shows the dimensional detail of the reentry capsule. The sonic line is located on the OREX-type configuration on the shoulder whereas in the case of the DART's reentry capsule as descried in the schematic sketch in Figure 1. The location of the sonic line is at the junction of the spherical blunt cone. Thus, it is noticed from the figure that the flow field over the reentry capsule needs a high aerodynamic drag with good static stability margin which leads to the selection of an axisymmetric shape of large angle sphere-cone combination. The fore-body geometry of the ARD module is having a spherical cap; the OREX capsule is having combination of the spherical cap with cone. The outer capsule consists of spherically blunted cone/fare. These capsules cover most of the existing reentry modules. Geometrical details of the ARD, Apollo, Apollo-II, MUSES-C, OREX and spherically blunted cone are displayed in Fig. 2. Table 1(b) summarized the geometrical parameters used in various spherically blunted-cone/flare reentry vehicles. (Fujimoto & Fujii, 2006) have numerically found that the shoulder radius has a great influence on the pressure

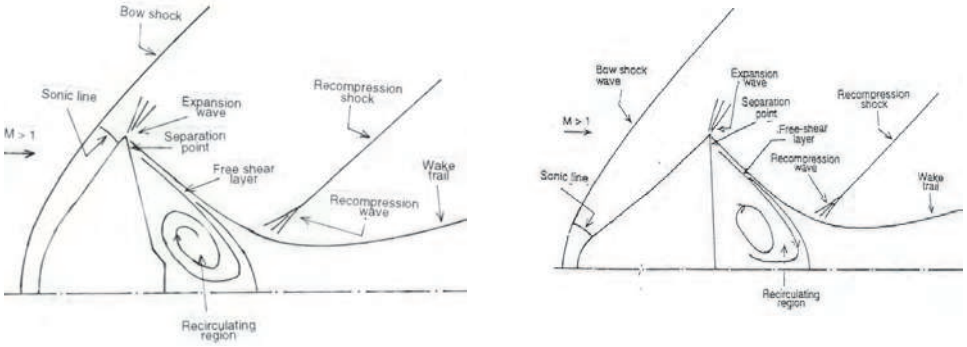

(a) flowfield over OREX capsule (b) flowfield over spherical blunt cone

Fig. 1. Representation of flow features on blunted body at supersonic speeds.

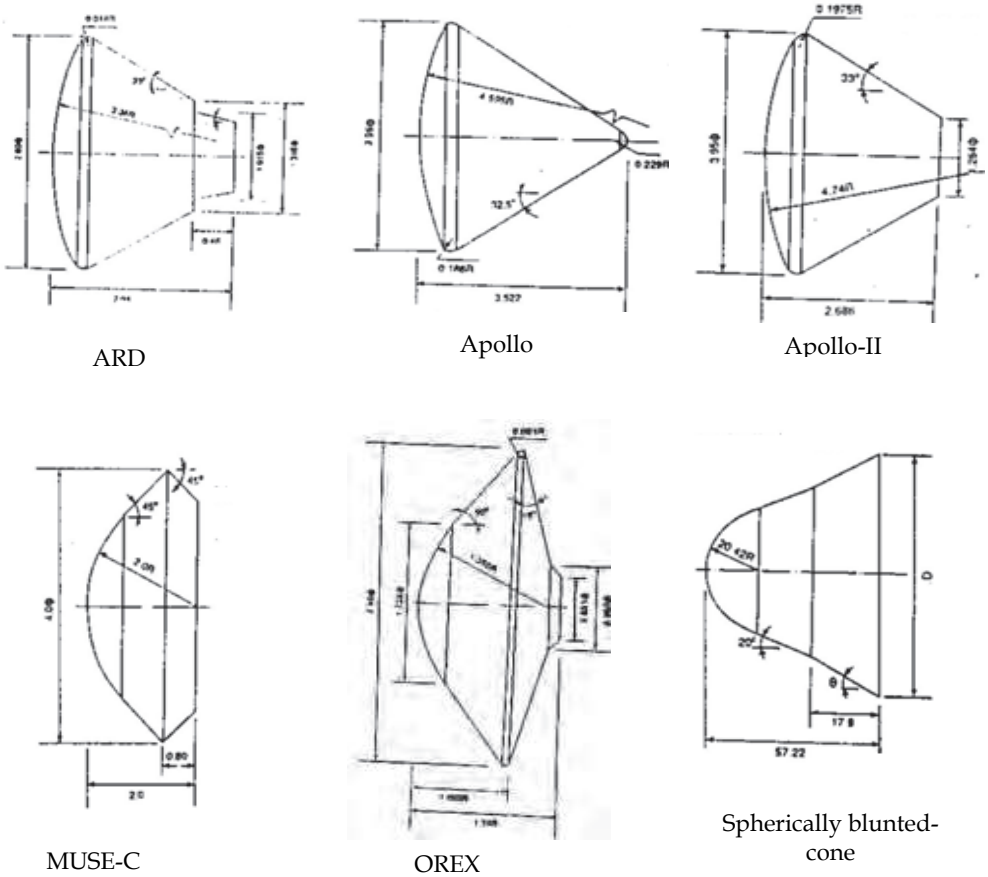

Fig. 2. Geometrical details of various reentry capsules.

Capsule	Spherical radius, R_N	Frontal diameter, D	Corner radius, R_C	Overall length, L	Semi-cone angle, α_N deg	Back-shell angle, α_B deg
ARD	3.36	2.80	0.014	2.04	–	33.0
Apollo	4.595	3.95	0.186	3.522	–	32.5
Beagle - 2	2.8	3.0	0.21	3.5	30	43
COMET	1.22	1.32	-	1.22	-	5
Apollo-II	4.74	3.95	0.1975	2.686	–	33.0
OREX smooth shoulder	1.35	3.40	0.001	1.508	50.0	15.0
OREX sharp shoulder	1.35	3.457	–	1.508	50.0	15.0
CARINA	1.97	1.0	0.25	1.172	–	13.0
Gemini	-	90.0	-	70.2	-	20
Project fire	70.2	58.79	-	38.86		33
Mars path finder	0.6638	2.6492	0.0662	70.19		46.63
Mercury	30	74.50	-	58.38	-	20
Viking	0.912	1.875	0.0914	2.0964	20	33.6
MUSES-C	2.0	4.0	–	2.0	45.0	45.0

Table 1. (a) Geometrical parameters of reentry capsules.

Base diameter, D	Semi-cone angle, θ
73.91	25
77.89	30
82.29	35

Table 1. (b) Geometrical parameters of spherically blunted cone reentry bodies.

level behind the body and separation position. Gnoffo et al. have found that laminar, wind-side heating levels may decrease with increasing angle of attack resulting from an increase in the effective radius of curvature with sonic line movement from the hemispherical nose to the aft shoulder of the blunt cone. Numerical simulation of the flow field is required over various geometrical parameters of the capsules in order to meet the aerodynamic and mission requirements. The numerical simulation of axisymmetric laminar compressible time dependent Navier-Stokes is carried out using a multi-stage Runge-Kutta time stepping scheme. A local time-step is used to simulate the flow over various reentry configurations.

2. Numerical schemes

Hypersonic calculations about complex geometries require large amounts of computer sources, but solution adaptive grids, convergence, acceleration, parallel processing may make run time manageable. The thin-layer approximation (Edwards 1992) is invoked, because viscous effects are generally present boundary layer near the wall. This

approximation neglects viscous derivatives in the directions tangent to the body surface, simplifying the equations somewhat alleviating grid resolution requirements. Numerical solution (Mehta et al., 1991) of the Navier-Stokes equations is obtained using Galerkin spatial discretiztion with multistage time integration. Table 2 depicts the various numerical schemes available to simulate the reentry flow field. Figure 3 shows the interlinking of computational fluid dynamics with the interaction of different discipline of sciences and engineering.

2.1 Algorithms

In the flux-splitting approach, the flux vector is separated into the sum of two vectors, one associated with the positive eigenvalues of the flux Jacobian, and the other with the negative values. Then appropriate one-sides differences can be used on the split terms. The main requirement being that the eigenvalues of the split flux Jacobian be positive or negative definite. The split fluxes are discretized with a one-sided difference scheme. This is analogous to adding dissipation to a central difference scheme where the dissipation increases near flow discontinuities such as shock waves, yielding improved stability.

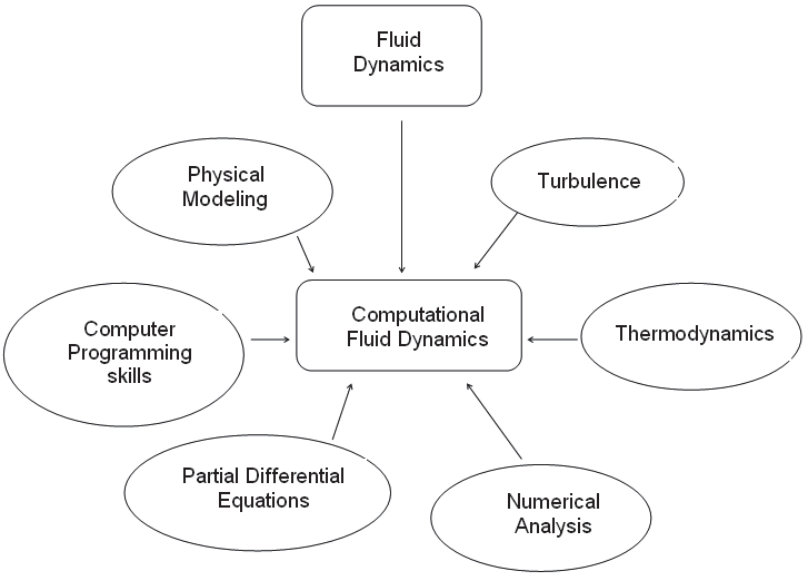

Fig. 3. Interaction of different area with CFD.

Riemann solvers are a class of schemes that propagate flow information according to solutions of Riemann problems. These schemes have the attributes of monotonicity, enabling sharp resolution of discontinuities, and robustness for capturing strong shocks. The one-dimensional inviscid problem can be solved exactly, but needs an expansive iterative approach, so most schemes are linearized, solve an approximate Riemann problem. The implicit numerical is allowed to have much higher time-step and having quadratic convergence. However the implicit algorithm needs computation of the Jacobian matrices of numerical fluxes, and having iterative solution of linear system. The implicit code is more

complicated as compared to explicit code. The numerical solution can be accelerated employing local time step, multi-grid, and preconditioning scheme.
CFD-FASTRAN code (Liever et al., 2003) is based on compressible finite volume solver for thermo-chemical non-equilibrium flow analysis. Roe's flux difference upwind scheme is used with the Van Leer flux limiter to provide higher-order spatial accuracy.

2.2 Air chemistry equations

The chemical behaviour of air depends on the trajectory points. Below about 2000 K, deviations from perfect gas behaviour are negligible. In the atmosphere, this temperature is first reached behind normal shocks at a Mach number of about six. Most of the test facilities are operated at low freestream temperatures and so real gas effects are difficult to obtain, even at high Mach numbers. The perfect gas equation of state is thus sufficient for many hypersonic speeds when the peak temperature is below the above limit. When the temperature in the flow is high enough to cause air to dissociate, the density of the fluid determines the character of the fluid/chemistry interaction. At relative high densities, the intermolecular collision rate is very high, and reactions proceed to equilibrium rapidly. The flow can be considered to be chemical equilibrium at all points in the flow field at all times as in the limit of infinite reaction rates. As the density is lowered, the chemical relaxation time increases and eventually becomes significant compared to the flow convection time. Air chemistry with numerical simulation is explained in details by (Edwards, 1992; and Gnoffo et al. 1989). (Rusanov, 1976) has reviewed fluid dynamics over reentry capsules. For a given thermodynamic state, the equilibrium composition of air is uniquely determined. Tables can be generated for the composition and properties of air in chemical equilibrium.
These tables with a linear interpolation or store the coefficients are used with flow solver. The perfect gas equation of state is modified by an effective specific heats ratio that is evaluated by table interpolation or curve evaluation. In the case of non-equilibrium air chemistry, the concentration of all the species should be known at all points in the flow field determined the properties of air undergoing chemical reactions. This requires solving additional transport equations for each species present in the flow. A source terms presents in the transport equations, accounts for the net production of the species arising in the chemical reactions. This term depends on the forward and backward rates of the reactions being modelled, which will differ with the gas species and reaction set of the gas model. The non-equilibrium gas model requires solving an additional set of partial differential equations, the number of equations being dependent on the number of species in the model.
In the frozen flow approximation (Hansen, 1959; Bailey 1967; & Srinivasan & Weilmuenster, 1987) individual species do not react with one another, but their effect is felt on the fluid dynamics because of variable thermodynamic properties and non-uniform concentration. Thus the species continuity equations are required. The computation time is saved due to not evaluating the production and destruction associated with chemical reactions. The flow is considered as a mixture of thermally perfect gases, with the specific heats and enthalpy of each species of the mixture determined as a function of temperature from a molecular data base.
A catalyst reduces the necessary activation energy of a reaction, hence more collisions level to reactions. The fully catalyst is equivalent to equilibrium of gases (thermal load). Poor catalyst reduces the release of reaction.

Numerical method	Combined space-time Discretization	Separate space discretization and time integration
Space-centered method	Explicit method (Lax & Friedrich, 1954) – First order (Lax & Wendroff, 1954) – second order	Implicit method (Briley & McDonald, 1975) (Beam & Warming, 1976)
	Two-step method (Richtmyer & Mortan, 1967) (MacCormack, 1969)	Explicit method Multistage Runge-Kutta schme (Jameson, Schmidt & Turkel, 1981)
	Implicit method (MacCormack, 1981)	
Upwind schemes	Flux vector splitting method (Moretti , 1979) - shock capturing (Steger & Warming, 1981) Exact Riemann problem solution (Godunov, 1959) – First order (Van Leer, 1979) – Second order Approximate Riemann solvers (Roe, 1981)	
High-resolution (non-linear schemes)	Explicit TVD upwind schemes (Boris & Book, 1973) (Harten, 1984) (Osher, 1984), (Oscher & Chakravarthy, 1984) Implicit TVD upwind schemes (Yee, 1985) Central TVD scheme (Implicit or Explicit) (Davis, 1984), (Roe, 1995)	

Table 2. Numerical method for Fluid Dynamics Equations.

3. Axisymmetric flow solver

The axisymmetric time-dependent compressible Navier-Stokes equations can be written in the following conservation form. The analysis is carried out under the assumption of laminar flow. The coefficient of molecular viscosity is calculated according to Sutherland's law. The temperature is related to pressure and density by the perfect gas equation of state. The ratio of the specific heats is assumed constant.

3.1 Finite volume method

To facilitate the spatial discretization in the numerical scheme, the governing equations are be written in the integral form over a finite volume of the computational domain with the boundary domain. The contour integration around the boundary of the cell is divided in the

anticlockwise sense. The computational domain is divided into a finite number of non-overlapping quadrilateral grids. The conservation variables within the computational cell are represented by their average values at the cell centre. When the integral governing equation is applied separately to each cell in the computational domain, we obtain a set of coupled ordinary differential equation.

3.1.1 Inviscid fluxes

The convective fluxes are calculated at the centre of the grid, resulting in cell-centre flux balances. The contour integration of the inviscid flux vector is approximated at the side of the computational grid. The summation is carried out over the four edges of the grid.

3.1.2 Viscous fluxes

The viscous terms are defined at the centre of the cell. The above procedure is repeated to approximate the contour integration of the viscous flux vector. The inclusion of diffusive transport terms requires a choice of the locations at which the derivatives of the primitive variables should be integrated. The grid used for gradient evaluation forms a second grid that is shifted a half cell in the axial and radial directions in relation to the original computational grid. The viscous flux vectors are approximated in such a manner to preserve cell conservations and maintain algorithm simplicity. The derivatives of primitive variables at the vertices of the cell are evaluated by discrete application of the divergence theorem (Peyret & Vivind, 1993) to the auxiliary cell of the secondary grid. The net convective flux is computed by summing the inviscid and viscous terms.

3.1.3 Artificial dissipation

In the cell-centered spatial discretization schemes, such as the one described above which is non-dissipative, therefore, artificial dissipation terms are added. The approach of (Jameson et al., 1981) is adopted to construct the dissipative terms consisting of blend of second and fourth differences of the vector conserved variables. Fourth differences are added everywhere in the flow domain where the solution is smooth, but are 'switched off' in the region of shock waves. A term involving second differences is then 'switched on' to damp oscillations near shock waves. This switching is achieved by means of a shock sensor based on the local second differences of pressure. Since the computational domain is structured. The scaling quantity confirms the inclusion of the cell volume in the dependent variable. The blend of second and fourth differences provides third-order back ground dissipation in smooth region of the flow and first-order dissipation in shock waves.

3.1.4 Time marching scheme

The spatial discretization described above reduces the governing flow equations to semi-discrete ordinary differential equations. The integration is performed employing an efficient multistage scheme (Jameson et al., 1981). The following three-stage, time-stepping method is adopted. A conservative choice of the Courant-Friedritchs-Lewy number (1.4) was made to achieve a stable numerical solution. The numerical algorithm is second-order accurate in space and time discretization. A global time step was used rather than the grid-varying time step to simulate time-accurate solution and is calculated as mentioned (Mehta, 2001).

3.1.5 Initial and boundary conditions

The freestream conditions for each trajectory point are enumerated in Table 3, which are used as initial conditions. The subscript ∞ represents freestream value in Table 3.

M_∞	U_∞, m/s	P_∞, Pa	T_∞, K
1.2	351	4519	210
1.4	409	3952	213
2.0	596	2891	219
3.0	903	2073	224
5.0	1532	1238	232
6.0	1890	1064	234

Table 3. Trajectory points and initial conditions.

Four types of boundary conditions are required for the computation of flow field, i.e. wall, inflow, outflow and symmetric conditions. They are prescribed as follows. At the solid wall, no-slip condition is enforced together with an isothermal wall condition. At the centre line of the symmetric reentry capsule are prescribed For the supersonic outflow case, all flow variables are extrapolated at the outer and wake region of the computational region.

3.2 Reentry capsule geometry

3.2.1 ARD capsule

The dimensional detail of the ARD capsule is having an axisymmetric design with a spherical blunt nose diameter, D = 2.8 m, spherical cap radius, R_N = 3.36 m and a shoulder radius, R_C = 0.014 m. The back shell has inclination angle α_N = 33 deg relative to the capsule's axis of symmetry. A frustum of cone of radius 0.0507 m with a 12 deg half angle cone is attached to the base region. The overall length of the capsule L = 2.04 m. The ARD resembles a 70% scaled version of the Apollo capsule (Liever et al. 2003).

3.2.2 OREX capsule

The OREX geometry is depicted in Fig. 2 with the detailed dimension. The fore-body shape consists of R_N = 1.35 m, a half-angle cone of α_N = 50 deg, D = 3.4 m, L = 1.508 m, and R_C = 0.01 m. The OREX geometry incorporates a rear cover with a small backward facing step at the junction between back cover and heat shield. The aft body is having α_B = 15 deg, half-angle cone relative to the plane of symmetry.

3.2.3 Beagle-2 capsule

The dimensional detail of the Beagle-2 in Table 1(a) is of axisymmetric designs. The fore-body of the Beagle has a 60 deg half cone with a maximum diameter, D = 0.9 m. The Beagle-2 capsule has a spherical blunt nose radius of R = 0.417 m, and a shoulder radius of R_C = 0.029m. The back shell has an inclination angle, α_B = 43.75 deg relative to the vehicle's axis of symmetry. The overall length of the module is L = 0.4995 m and the length to the diameter ratio is 0.555.

3.2.4 Apollo capsule

The dimensional detail of the Apollo is shown in Fig. 2 are of axisymmetric designs. The Apollo capsule has a spherical blunt nose diameter of D = 3.95 m, spherical nose radius of α_N = 4.595 m and a shoulder radius of R_C = 0.186 m. The back shell has an inclination angle, α_B = 32.5 deg relative to the vehicle's axis of symmetry. The overall length of the module is L = 3.522 m.

3.2.5 Spherically blunted-cone/flare capsule

The spherically blunted-cone/flare configuration is illustrated in Fig. 2. The conical fore-body has R_N = 0.51 m, D = 2.03 m, L = 1.67 m and α_N = 20 deg. The flare has a half-angle cone of 25 deg and is terminated with a right circular cylinder and a geometrically similar to the REV of the DART demonstrator. Table 1(b) gives the semi-cone angle of various reentry vehicles.

3.3 Computational grid

One of the controlling factors for the numerical simulation is the proper grid arrangement. The following procedure is used to generate grid in the computational region of the blunted-body. The computational domain is divided into number of non-overlapping zone. The mesh points are generated in each zone using finite element method (Mehta, 2011) in conjunction with the homotopy scheme (Shang, 1984). The spiked blunt nosed body is defined by a number of grid points in the cylindrical coordinate system. Using these surface points as the reference nodes, the normal coordinate is then described by the exponentially stretched grid points extending outwards up to an outer computational boundary.

Grid independence tests (Mehta, 2006; and Mehta 2008) were carried out, taking into consideration the effect of the computational domain, the stretching factor to control the grid intensity near the wall, and the number of grid points in the axial and normal directions. The outer boundary of the computational domain is varied from 2.5 to 3.0 times the maximum diameter D and the grid-stretching factor in the radial direction is varied from 1.5 to 5. These stretched grids are generated in an orderly manner.

Fig. 4. Comparison between density contour and schlieren picture.

To verify the chosen grid delivers an accurate solution, the number of grid cells was increased until a steady-state solution occurred, that is, the resulting axial force on the investigated shape did not change anymore. Several test runs were made with a total doubled grid cell number. Therefore, the grid was highly refined in both directions. Grids are chosen with the number of grid points in the axial direction ranging from 187 for the shortest capsule to up to 220 for the longest reentry configuration, and the number in the radial direction ranging from 52 to 82. The present numerical analysis was performed on 187x62 grid points. The downstream boundary of the computational domain is maintained at 4 to 6 times the maximum diameter, D. This grid arrangement is found to give a relative difference of about ±1.5% for the drag coefficient. The convergence criterion less than the 10^{-5} is based on the difference in the density values at any grid point between two successive iterations. The minimum spacing for the fine mesh is dependent upon the Reynolds number. The finer mesh near the wall helps to resolve the viscous effects. The coarse-mesh helps reducing the computer time. It is important that the grid have sufficient points in the shoulder region of the reentry module in order to capture the rapid expansion and accurately predict the flow separation point and the angle of the resulting shear layer. A close-up view of the computational grid over the various reentry capsules is shown in Reference (Mehta, 2010). The structured grid generation and the mono block are suitable to accommodate spike shape. As seen in the figures of (Mehta, 2006; Mehta 2010), these types of grid use quadrilateral cells in 2-D in the computational array. The quadrilateral cells, which are very efficient at filling space, support a high amount of skew and stretching before the solution will be significantly affected. Additionally, the grid can be aligned with the flow, thereby yielding greater accuracy within the solver. Several grid arrangements are take check the grid independency check.

3.4 Flow characteristics

The flow field features over various capsules have been shown by (Mehta, 2010). Figure 4 shows the comparison between the density contour and schlieren picture for spherical blunted-cone at $\theta = 25$ deg configuration at $M_\infty = 6.0$. All the essential flow field features are well captured and compared well with the schlieren picture. Figure 4 depicts the velocity vector plots for Apollo, Apollo-II and ARD reentry modules. It can be visualized from the vector plots that all the significant flow field behaviors such as bow shock wave, rapid expansion fans and the flow at the shoulder, flow recirculation region with converging free shear layer and formation of the vortex flow in the aft region of the capsules. The wake flow field immediately behind the vehicle base, exhibits complex flow characteristics. The formation of the bow shock wave on the fore body depends on R_N and α_N and M_∞. The bow shock wave moves close to the fore body with the increasing M_∞ and the stand off distance between the bow shock wave and the fore body decreases with the increasing M_∞.

The pressure, density and Mach contour plots show the enlarged view of the computed vector field over the OREX, ARD, Apollo at various freestream Mach number M_∞. It can be visualized from the vector plots that all the significant flow field features such as bow shock wave, rapid expansion fans on the shoulder of the capsule, flow recirculation region with converging free shear layer and formation of the vortex flow in the aft region of the capsules. The wake flow field, immediately behind the capsule base, exhibits complex flow characteristics. The formation of the bow shock wave on the fore body depends on R_N and α_N and M_∞. In the case of spherically blunted-cone/flare (SRE) capsule, the bow shock wave does not follow the body contour, which is attributed to small values of R_N and α_N as compared to the OREX, the ARD and the Apollo.

Computed vector velocity plot around the various vehicles are depicted in Fig. 5. The Mach contour plots show the formation of vortices at the corner region of the capsule for $M_\infty \leq 3$. Characteristics flow features around the blunt body at supersonic speeds is observed. The high surface pressure on the fore-body results the development of high aerodynamic drag which is required for the aerobraking application. Table 4 shows the fore body aerodynamic drag for various reentry modules. It is important to mention here that the aerodynamic drag is highly influenced by the fore body shape.

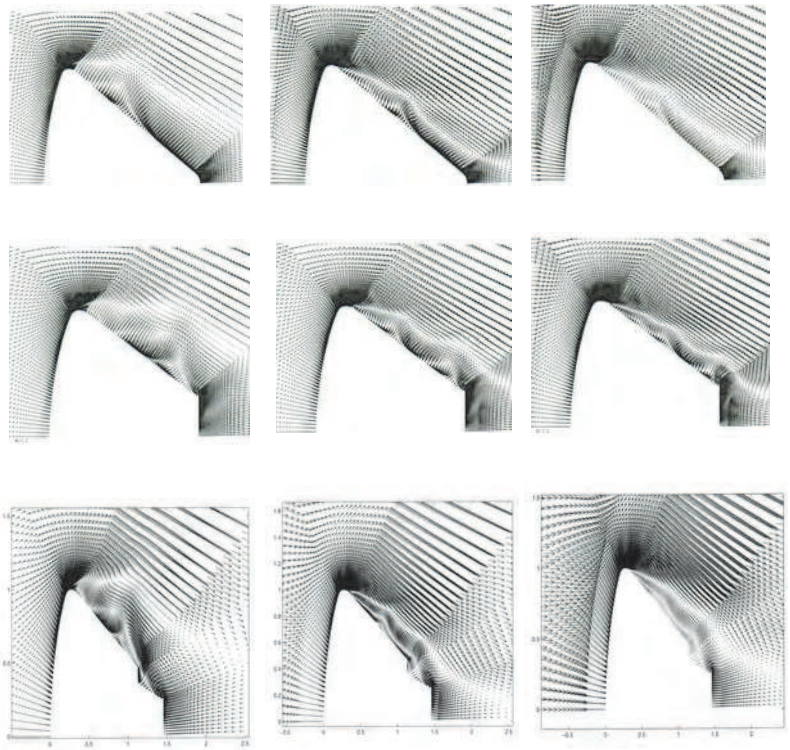

Fig. 5. Enlarged view of velocity vector field over Apollo, Apollo-II and ARD.

3.5 Shock stand-off distance

The computed velocity vector plots are shown in Fig. 6. Close-up views of the velocity vector plot over fore-body of the capsules and schematic shock location are depicted in the figure. The separated shear layer and the recompression shock from the reattachment point on the shoulder of the hemispherical cap are visible in the vector plot. The shock wave in front of the cap will increase the aerodynamic drag due to high pressure region. In the fore region of the spherical cap, the fluid decelerates through the bow shock wave. At the shoulder of the disk or hemispherical cap, the flow turns and expands rapidly, the boundary layer detaches, forming a free shear layer that separates the inner recirculating flow region behind the base from the outer flow field. The corner expansion over disk process is a modified Prandtl-Mayer pattern distorted by the presence of the approaching boundary layer.

Capsules	M_∞ =1.2	M_∞=1.4	M_∞=2.0	M_∞=3.0	M_∞=5.0	M_∞=6.0
ARD	1.41	–	1.43	1.40	1.38	–
Apollo	1.30	–	1.50	1.43	1.40	–
Apollo – II	1.32	–	1.47	1.43	1.05	–
OREX (with smooth shoulder)	1.79	1.77	1.50	1.30	1.16	–
OREX (with sharp shoulder)	1.80	1.66	1.36	1.17	1.05	–
CARINA	1.40	–	1.50	1.45	1.45	–
MUSSES – C	1.27	–	1.24	1.36	1.38	–
Beagle – 2	1.58	1.59	1.54	1.47	1.42	–
Spherically blunted cone, θ=25 deg	0.40	–	0.43	0.44	–	0.42
Spherically blunted cone, θ=30 deg	0.51	–	0.49	0.46	–	0.42
Spherically blunted cone, θ=35 deg	0.58	–	0.56	0.51	–	0.47

Table 4. Fore-body aerodynamic drag.

For the case of flat-nosed capsule flying at hypersonic speeds, a detached bow wave is formed in front of the nose which is practically normal at the body axis (Truit, 1959; Liepmann & Roshko 2007). Since the flow behind the normal shock is always subsonic, simple continuity considerations show that the shock-detachment distance and stagnation-velocity gradient are essentially a function of the density ratio across the shock. The flow behind the shock wave is subsonic, the shock is no longer independent of the far-downstream conditions. A change of the spike shape (geometry) in the subsonic region affects the complete flow field up to the shock. The shock-detachment distance becomes smaller with increasing density ratio. (Hayer & Probstein 1959) gives expression for the shock detachment distance Δ_F with diameter of the flat-disk D_S ratio as

$$\frac{\Delta_F}{D_S} = 2.8\sqrt{\frac{\rho_\infty}{\rho_0}} \tag{1}$$

where the density ratio across the normal shock (Ames Research Staff, 1953) is

$$\varepsilon = \frac{\rho_\infty}{\rho_0} = \frac{(\gamma-1)M_\infty^2 + 2}{(\gamma+1)M_\infty^2} \tag{2}$$

The ratio of shock stand-off distance Δ_S with hemispherical cap of diameter, D_S is

$$\frac{\Delta_S}{D_S} = \frac{2\varepsilon}{1+\sqrt{\frac{8\varepsilon}{3}}} \tag{3}$$

The values of Δ_F/D_S and Δ_S/D_S are found 0.1898 and 0.1109, respectively. The numerical values of the ratio of shock stand-off to cap diameter are calculated from the velocity

vector and pressure contour plot and they are 0.19 and 0.11 which show good agreement with the analytical values. The spherical spike shows the greatest change in velocity gradient as compared to the flat disk. The flow is compressed to subsonic condition, which appears as inviscid and incompressible (Truit, 1959; Liepmann & Roshko 2007) . The shock wave stands in front of the blunt body and forms a region of subsonic flow around the stagnation region.

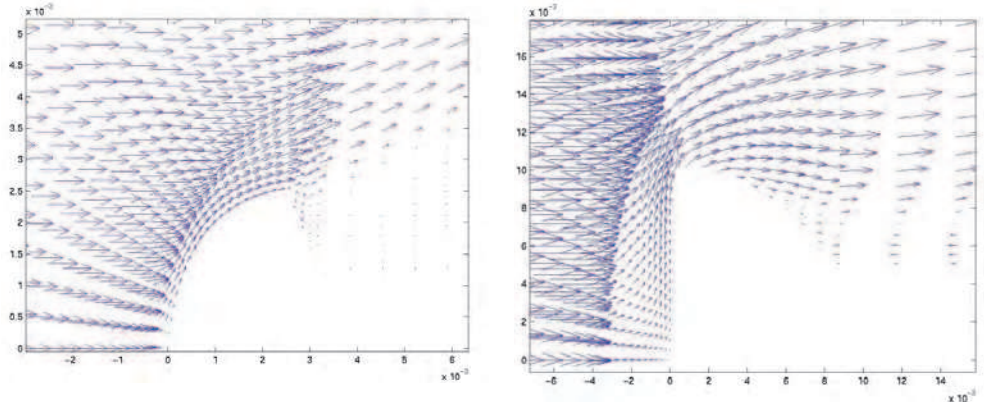

(a) Hemispherical forebody (b) Flat-disc forebody

Fig. 6. Close-up view of Velocity vector plot over fore body of the capsules.

3.6 Wall heat flux

The inviscid flow field in the vicinity of the stagnation point is described in a fluid dynamics sense as the conversion of a unidirectional high velocity stream by a normal shock wave into a high temperature subsonic layer, which is taken to be inviscid and incompressible (Truit, 1959). The stagnation point of a blunt body, the incoming hypersonic flow brought to rest by a normal shock and adiabatic compression. The heat transfer rate is directly proportional to the enthalpy gradient at the wall and square root of the tangential velocity gradient at the edge of the boundary layer. The inviscid flow field in the vicinity of the stagnation point is described as the conversion of the uni-directional, high velocity stream by a normal shock wave into a high temperature subsonic layer. The enthalpy gradient is determined by the shape of the velocity profile in the boundary layer and by the variation of the air properties with temperature. Heat flux at the stagnation point can be calculated using following expression of (Fay & Riddle, 1958)

$$q_w = 0.763\,\mathrm{Pr}^{-0.6}\sqrt{(\rho_\infty \mu_\infty K)}\sqrt{\left(\frac{\rho_w \mu_w}{\rho_\infty \mu_\infty}\right)}(h_\infty - h_w) \tag{4}$$

where the subscripts ∞ and w are freestream and wall, respectively. Pr is Prandtl number, K stagnation point velocity gradient and h enthalpy of air. The value of stagnation point velocity gradient K is taken as 0.3 (White, 1991). The hemispherical spike shows the greatest changes in the velocity gradient as compared to the flat disk spike. The magnitude of the stagnation-velocity gradient indicates the maximum heat transfer over the hemispherical

spike. The computed values of the stagnation point heat flux are 0. 556×10^7 W/m^2 and 1.45x10^7 W/m^2 for the flat-disk and the hemispherical disk spike, respectively. The stagnation point calculated using Eq. (4) is 0. 831x10^7 W/m^2 and 1.55×10^7 W/m^2 for the flat-disk and the hemispherical disk spike, respectively. The discrepancy is due to value of the K. The value of K is difficult to calculate for the flat disk (Bertin, 1994). The results show reasonably good agreement between them. Close-up view of velocity vector plot over the blunt body gives a comparative velocity gradient. The velocity vector is turning in the stream line fashion on the hemispherical spike where as on the flat-disk of the reentry modules as appears that the flow is impinging.

3.7 Oscillation flow field characteristics

The oscillation motion is noticed in the numerical simulations. The flow field can be visualized in the instantaneous velocity vector plots. One oscillation cycle is corresponding to approximately 0.12s for the Apollo and 0.96s for the OREX capsule. For the sake of brevity we are displaying one flow cycle in the six time intervals of 0.002s and 0.16s for the Apollo and the OREX capsules, respectively. Figures 6 and 7 show the close-up view of the computed instantaneous velocity vector field over the Apollo and the OREX modules at M_∞ = 1.2. It can be observed from the vector plots that all the significant flow field features such as bow shock wave ahead of the capsule, rapid expansion fans on the corner, flow recirculation region with converging free shear layer and formation of the vortex flow in the aft region of the capsule.

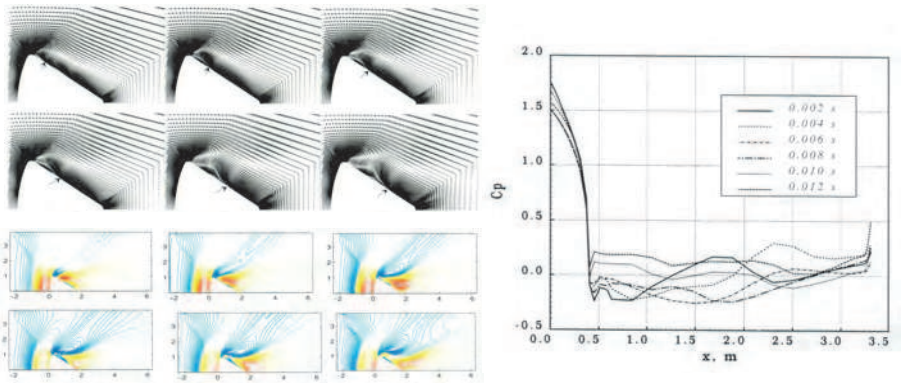

Fig. 7. Instantaneous vector field, pressure contour plots and wall pressure distribution over Apollo capsule.

The wake flow field immediately behind the capsule base exhibits complex flow characteristics. It is also seen that the formation of the bow shock wave on the fore-body of the capsules and which depends on the R_N, R_C and α_B. A gradual flow turning can be observed in Fig. 7 for the case of Apollo which is having smooth shoulder of radius R_C = 0.01 m. The approaching supersonic boundary layer separates at the corner and free shear layer is formed in the wake region. The wake flow features also depicts vortex attached to the corner with a large recirculating flow behind the capsule adjacent to the axis of symmetry which depends on back shell cone angle. The separation point moves downstream zone and location of vortex depend on time as can be visualized from the vector and density contour plots.

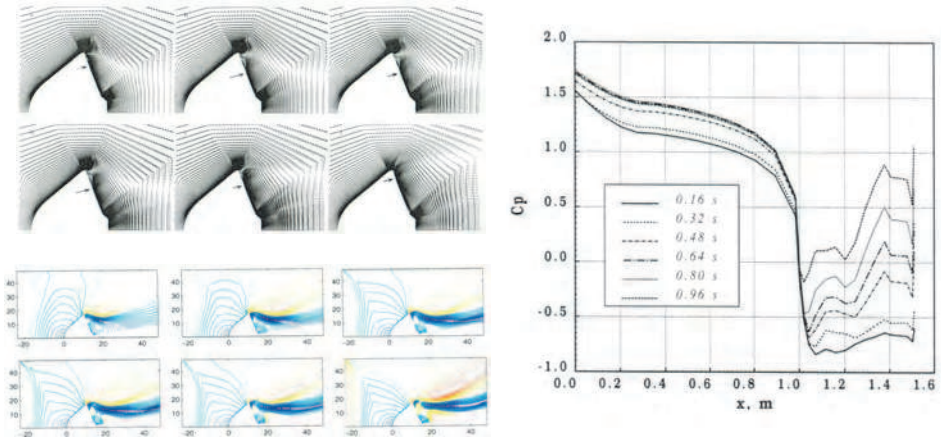

Fig. 8. Instantaneous vector field, pressure contour plots and wall pressure distribution over OREX capsule.

Computed instantaneous Mach contour plots over the Apollo and the OREX capsules are also depicted in Figs. 7 - 8. It can be observed from the contour plots that the oscillatory motion of the flow field in the base region of the flow capsules. Vortices are generated at the capsules and are changing location as a function of time. The flow structure inside the recirculating region is influenced by the periodic motion of the separation bubble and the vorticity of the flow.

The periodic phenomenon is analyzed using the surface pressure variation over the capsules. The figures also show the pressure coefficient Cp variation over the Apollo and the OREX modules. The x = 0 location is the stagnation point. The sonic point moves to the corner of the blunt bodies and affects the pressure distribution throughout the subsonic flow. The pressure coefficient shows over expanded flow in the case of the OREX module. These types of flow field features are also explained by (Bertin, 1994) in conjunction with the flow past reentry capsule. A sudden drop of Cp is noticed on the shoulder of the module followed by a negative pressure variation in the base region. A low pressure is formed immediately downstream of the base which is characterized by a low speed recirculation flow region which can be attributed to fill-up the growing space between the shock wave and body. In the base region, the Cp is increasing with time interval of the cycle. The effect of the shoulder radius of the capsule on the Cp can be seen in the figures. The Apollo capsule is having small conical angle at the base-shell as compared to the OREX base-shell geometry of semi-angle cone of 75 deg. The pressure over the fore body of the capsules is varied with time. Thus, the cyclic of the flow field in the base region is influenced the fore body flow. The different base-shell cone angles give significant effects in the time period. A wavy pattern is seen in the pressure distribution in the base region which may be attributed to complex geometry in the base region. The periodicity of the flow field in the base region are 0.12s (8.33 Hz) and 0.096s (1.04 Hz) for the Apollo and the OREX modules, respectively. It is important to say that the cycle of the flow field over the OREX is 8 times slower than the Apollo. Comparing the computed base-pressure with a common engineering formula (Bonner et al., (1989).

$$\Delta C_{D,base} = \frac{1}{M_\infty^2} - \frac{0.57}{M_\infty^4} \tag{5}$$

The relation is useful to determine the base drag of the capsule as well as to validate the numerical results.

4. Three-dimensional Navier-Stokes equations

The reentry capsule considered here is typified by the Apollo command module. This shape encompasses most of the problems that arises from both viscous and inviscid flow field considerations. The module is at an arbitrary angle of attack that achieved by an offset centre of gravity relative to the free-stream flow. Thus, though the body is axisymmetrical, the geometry of the flow field is not. The only plane of symmetry is the pitch plane, which contains the free-stream velocity vector and the body axis. The bow shock wave in front of the body is fully detached; a subsonic region exists behind the shock wave on the front side of the capsule. As the flow expands around the body, a sonic surface is created (Mach = 1); since the flow continues to increase in speed, it becomes supersonic downstream of this surface. At the downstream the boundary layer tends to separate. The details of the flow vary with geometry and freestream conditions, the general flow features remain the same. The fore body flow field is dominated by a strong bow shock wave. As the flow turns around the shoulder of the reentry module it rapidly expands and can separate. The leeward side flow separates just after the shoulder, whereas the windward side flow remains attached until the rear apex. A shear layer separates the outer flow from the recirculating inner core, which contains multiple counter rotating vortices. The separation shear layer eventually coalesces, forming the neck or narrowest point in the wake. A wake shock is formed at that point, which compresses the flow, leading to local maxima in pressure and temperature. Further away from the neck is far wake region, which extends for many body diameters downstream as the momentum deficit created by the passing module is slowly recovered. Emanating from the separation regions the dividing stream surface, that defines the boundary of the recirculation region – an area in which the flow is trapped. The flow field outside the dividing stream lines proceeds to a single flow stream at the neck of the wake. Oblique shocks are generated near the neck because of the flow external to the wake is turned supersonically. The surrounding inviscid flow and the viscous mixing layer flow build up in the wake much like a boundary layer and develop into the far wake downstream of the base flow field.

4.1 Three-dimensional Euler equations

The flow field analysis over various reentry configurations is studied numerically by solving time-dependent compressible Euler equations. The governing fluid flow equations are discretized in spatial coordinates employing a finite volume approach, which reduces the equations to semi-discretized ordinary differential equations. Temporal integration is performed using multi-stage Runge-Kutta time stepping scheme. A local time step is used to achieve steady state solution. The numerical computation is carried out for freestream Mach number of 10.0 and angle of attack of 10.0 degree. The flow features around the blunt body are characterized by a bow shock wave, expansion wave and base flow region. The numerical scheme captures all the flow field features well. Comparisons of the flow field and surface pressure distribution results are made between different configurations of the

blunt body capsules such as ARD (ESA's Atmospheric Reentry Demonstrator), Apollo II, MUSES-C, OREX (Orbital Reentry EXperiments) with and without shoulder curvature and spherically blunted cone with flare angle of 30 and 35 degree. The inviscid analysis takes into consideration centrifugal force and expansion fan at the shoulder of the reentry capsules. The effects of the capsule geometry on the flow field may be useful for optimization of the reentry capsule. The Newtonian flow assumptions are used to calculate forebody aerodynamic drag for various blunt-bodies in conjunction with the NISA software. A comparison between CFD and the Newtonian flow assumptions for various reentry modules are made, and comparison shows an agreement between them. The numerical scheme is described in detail in References (Mehta & Tiwari, 2008; Mehta, 2007).

A finite volume cell is specified by eight corners, which are connected by straight lines. Figure 9 shows hexahedral cell in the computational domain. The discrete values of the flow quantities are calculated at the centre of the cell. The surface integral) over the convective part of the flux density tensor is evaluated for each component cell using an arithmetic average of the flux quantities at the vertices to determine the values on each of the cell faces. Then, the resultant convective inflow of mass, momentum, energy associated with cell centre point is computed by summing the contributions of the component cells. Any open-surface element for a given boundary has a unique, effective surface vector S that is independent of the shape of the surface. This is because, by applying the divergence theorem to a constant vector, the integral of the outward-oriented surface normal over a closed surface vanishes. For instance, the surface vector S-5678 is independent of the choice of which partitioning surface diagonal is used to define the cell volume with vertices 1 to 8. Whether the four vertices are on a plane or not, the surface vector is equal to one-half the cross product of its diagonal line segment. Given eight arbitrary corner points prescribing a general hexahedral, a simple way to define a shape whose volume can be precisely calculated is to partition each face into two planar triangles. The volume is then dependent on which diagonal is used on each face. The volume is the dependent on which diagonal is based on each face, since the diagonal of four non-planar points do not intersect. (Kordulla & Vinokur, 1983) had been used here to calculate cell volume.

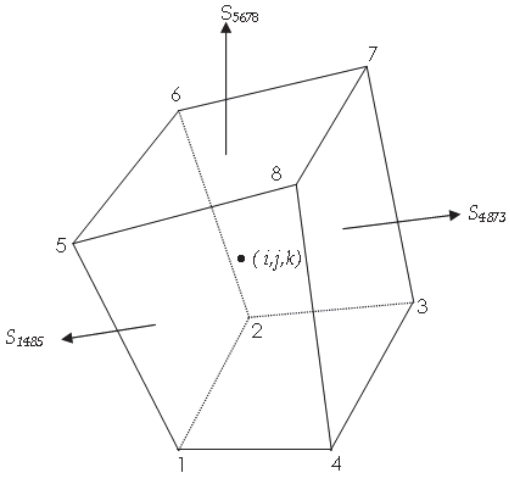

Fig. 9. A hexahedral computational grid of point (i,j,k).

4.2 Flow field over vehicle at angle of attack

Figure 10 shows the Mach contour plots over the OREX and Apollo modules. For the sake of brevity we are presenting windward and leeward sides flow field over OREX with smooth and without smooth shoulder, ARD, Apollo II and spherical-cone configurations are shown at M = 10.0 and at angle of attack 10.0 degree in Fig. 10. The Mach contour plots display the flow field in the windward and the leeward side of the capsules. A shock wave stands in front of the reentry blunt body and forms a region of subsonic flow around the stagnation region. Characteristic features of the flow field around the blunt body at high speed, such as bow shock wave ahead of the capsule and the expansion waves on the shoulder of the capsules. The bow shock wave follows the body contour and the fore body is entirely subsonic up to the corner tangency point of the ARD, the Apollo and the OREX where the sonic line is located. In the case of the spherically blunted cone-flare module, the sonic line is located at the junction of the sphere cone as seen in the Mach contour plots. The flow expands at the base corner. The flow field over the reentry modules became complicated due to the presence of corner at the shoulder and the base shell of the capsule as delineated in the Mach contour plots. Detailed flow field analysis is presented in (Mehta 2007). It is found at the transonic flow cases that a steady state solution could not be achieved due to unsteady nature of the base flow. Table 5 shows the aerodynamic drag numerically computed for COMET and Beagle-2 reentry modules.

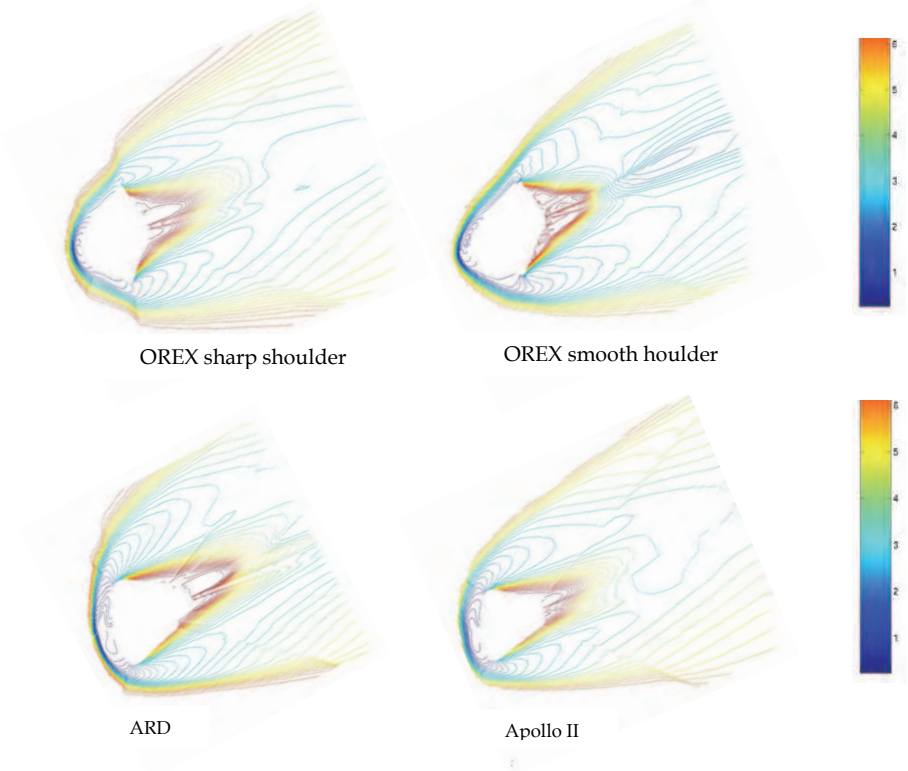

Fig. 10. Mach contour plots over reentry capsules at M = 6.0 and angle of attack 5 deg.

Capsules	M_∞=1.5	M_∞=2.0	M_∞=3.0	M_∞=5.0	M_∞=7.0
COMET	1.56	1.55		1.49	–
Beagle – 2	1.48	1.50	1.502	1.508	1.482

Table 5. Numerically computed aerodynamic drag coefficient.

4.3 Newtonian impact theory

In the Newtonian flow concept the shock wave is assumed to coincide with the body surface. It is also assumed that the freestream maintain its speed and direction unchanged until it strike the surface exposed to the flow. The impact theory does not specify the pressure on surface that do not "visualize" the flow, that is, the surfaces on which gas dynamics would predict Prandtl-Mayer flow. When the flow is curved in the direction of freestream, the difference in pressure from the shock wave to the body surface equals the centrifugal force, due to the curvature of the flow.

A computer program is written to compute the aerodynamic coefficients using the modified Newtonian sine-squared law $C_p = C_{p,max} \sin^2\theta$, where θ is the angle between the freestream velocity vector, and $C_{p,\ max}$ maximum pressure coefficient, which is calculated at a stagnation point behind a normal shock using the Rayleigh pitot tube formula for frozen gas chemistry (constant specific ratio of heats). (Lees, 1955) proposed a modified Newtonian theory, which consists in scaling down so as to be exact at stagnation point, where the correct value is known. The forebody aerodynamic drag is also computed using Newtonian flow assumptions. The numerical simulation can be validated with the post flight data of the Gemini, Apollo and Star dust flights data (Griffith, 1967; Griffith & Boylan, 1968; Lockman, 1970; & Wood, 1997).

5. Conclusion

The aerodynamic characteristics of the reentry capsules are studied experimentally employing the shock tube, the high enthalpy tunnel, wind-tunnel, and free-flight testing. The experimental set up has to design to meet the specific requirements and conditions for the reentry probes. The post flights test data are available for many reentry modules. The flow fields over many reentry modules are generated using computational fluid dynamics for various test conditions. The computational fluid dynamics can be used to analyze and understand the complex flow field features in the wake region of the modules. Numerical simulation can be used to get aerodynamic characteristics, wall heat flux, and stability margin for the optimization of the trajectory of the capsules.

6. Acknowledgment

The author is indebted to his parents and Vikram Sarabhai Space Centre, Trivandrum, India for their valuable encouragement, help and contributions to build the research career.

7. References

Allen, J. S. and Cheng, S. I. (1970). Numerical solution of the compressible Navier-Stokes equations for the near wake, Physics of Fluids, Vol. 13, No. 1, pp. 37-52

Ames Research Staff (1953). Equations, tables and charts for compressible flow, NACA report 1135

Beam, R. M., and Warming, R. F. (1976). An implicit finite-difference algorithm for hyperbolic systems in conservation law form, Journal of Computational Physics, Vol. 22, pp. 87-110.

Bedin, A. P., Mishin, G. I., and Chistyakove, M. V. (1992). Experimental investigation of the aerodynamic characteristics and geometric parameters of flows about various molecular structures, in "Gas Dynamics" edited by Yu. I. Koptev, Nova Science Publishers, N.Y., pp. 39-67

Bertin, J. J. (1994). *Hypersonic Aerothermodynamics*, AIAA Education Series, AIAA Press, VA, USA

Bonner, E., Clever, W., and Dunn, K. (1989). Aerodynamic preliminary analysis system II, part I – theory, NASA CR 165627

Briley, W. R., and McDonald, H. (1975). Solution of the tree-dimensional compressible Navier-Stokes equations by an implicit technique, Proceedings of Fourth International Conference on Numerical Methods in Fluid Dynamics, Lecture Notes in Physics, Vol. 35, Springer-Verlag, Berlin

Bailey, H. E.(1967). Programs for computing equilibrium thermodynamic properties of gases, NASA TN D-3921

Boris, J. P., and Book, D. L. (1973) Flux corrected transport 1, SHASTA, a finite transport algorithm that works, Journal of Computational Physics, Vol. 11, pp. 38-69

Chester, W. (1956). Supersonic flow past a bluff body with a detached shock, Journal of Fluid Mechanics, Vol. 1, pp. 353-365

Davis, S. F. (1984) TVD finite difference schemes and artificial viscosity, NASA CR-172373.

Edwards, T. A. (1992). Fluid/chemistry modeling for hypersonic flight analysis, Computers Mathematical Applications, Vol. 24, No. 5/6, pp. 25-36

Fay, J. A., and Riddle, F. R. (1958). Theory of stagnation point heat transfer in dissociated air, Journal of Aeronautical Sciences, Vol. 25, pp. 73-85

Freeman, N. C. (1956). On the theory of hypersonic flow past plane and axially symmetric bluff bodies, Journal of Fluid Mechanics, Vol. 1, pp. 366-387

Fujimoto, K., and Fujii, K. (2006). Computational aerodynamic analysis of capsule configurations toward the development of reusable rockets, Journal of Spacecraft and Rockets, Vol. 43, No. 1, pp. 77-83

Gnoffo, P. A., Weilmuenster, K. J. (1996). Braun, R. D., Cruz, C. I., Influence of sonic-line location on Mars Pathfinder probe aerothermodynamics, Journal of Spacecraft and Rockets, Vol. 33, No. 2, pp. 169-173

Gnoffo, P., Gupta, R., and Shinn, J. (1989). Conservation equations and physical models for hypersonic air flows in thermal and chemical non-equilibrium, NASA TP-267

Godunov, S. K. (1959). A difference scheme for numerical computation of discontinuous .solution of hyperbolic equations, Math. Sb., Vol. 47, pp. 271-306

Grasso, F. and Pettinelli, C. (1995). Analysis of laminar near wake hypersonic flow, Journal of Spacecraft and Rockets, Vol. 32, No. 6, pp. 970-980

Griffith, B. J. (1967). Comparison of aerodynamic data from the Gemini flights and AEDC-VKF wind tunnels, Journal of Spacecraft and Rockets, Vol. 4, No. 7, pp. 919-924

Griffith, B. J., and Boylan, D. E. (1968). Post flight Apollo command module aerodynamic simulation tests, Journal of Spacecraft and Rockets, Vol. 5, No. 7, pp. 843-848

Haas, B. L. and Venkatapathy, E. (1995). Mars path finder computations including base heating predictions, AIAA 95-2086

Harten, A. (1984). On a class of high resolution total variation stable finite difference schemes, SIAM Journal of Numerical Analysis, Vol. 21, pp. 1-23

Hansen, C.F. (1959). Approximations for the thermodynamic and transport properties of high temperature air, NASA TR R-50

Hiraki, K., Inatani, Y., Ishii, N., Nakajima, T., and Shimoda, T. (1998). Dynamic stability of MUSES-C capsule, 21st International Symposium on Space Technology and Science, Report ISTS-98-d-33

Hayer, W. D. and Probstein, R. F. (1959). *Hypersonic Flow Theory*, Academic Press, New York

Jameson, A., Schmidt, W., Turkel, E. (1981). Numerical solution of Euler equations by finite volume methods using Runge-Kutta time stepping schemes, AIAA paper 81-1259

Kordulla, W. and Vinokur, M. (1983). Efficient computation of volume in flow predictions, AIAA Journal, Vol. 21, No. 6, pp. 917-918

Lamb, J. P. and Oberkampf, W. L. (1995). Review and development of base pressure and base heating correlations in supersonic flow, Journal of Spacecraft & Rockets, Vol. 32, No. 1, pp. 8-23

Lax, P. D., (1954). Weak solutions of nonlinear hyperbolic equations and their numerical computation, Communications in Pure and Applied Mathematics, Vol. 7, pp. 159-193

Lax, P. D., and Wendroff, B. (1954). Systems of conservation laws, Communications in Pure and Applied Mathematics, Vol. 15, pp. 363-388

Lees, L. (1955). *Hypersonic flow*, Institute Aeronautical Science, Preprint No. 554

Liever, P. A., Habchi, S. D., Burnell, S. I. and Lingard, J. S. (2003). Computational fluid dynamics prediction of the Beagle 2 aerodynamic data base, Journal of Spacecraft and Rockets, Vol. 40, No. 5, 2003, pp. 632-638

Liepmann, H. W., and Roshko, A. (2007). *Elements of Gas Dynamics,* 1st South Asian Edition, Dover Publications Inc, New Delhi

Lighthill, M. J. (1957). Dynamics of a dissociating gas, Part 1: Equilibrium flow, Journal of Fluid Mechanics, Vol. 2, pp. 1-32

Lockman, W. K. (1970). Base-heating measurements on Apollo block II command module, Journal of Spacecraft and Rockets, Vol. 7, No. 1, pp. 93-94

MacCormack, R. W., (1969). The effect of viscosity in hyper-velocity impact cratering, AIAA paper 66-354

MacCormack, R. W., (1981). A numerical method for solving the equations of compressible viscous flow, AIAA paper 81-0110

Menne, S. (1994). computation of non-winged vehicle aerodynamics in the low supersonic range, in the proceedings of the 2nd European Symposium on Aerothermodynamics for Space Vehicles, ESTEC, Noordwiik, The Netherlkands, 21-25 November, pp. 73-78

Mehta, R. C. (2006). Computational investigation of flow oscillation over reentry capsules, Computational Fluid Dynamics JOURNAL, Vol. 15, No. 2, pp. 247-260

Mehta, R. C. (2006). Numerical simulation of supersonic flow past reentry capsules, Shock Waves, Vol. 15, No. 1, pp. 31-41

Mehta, R. C., Jayachandran, T., and Sastri, V. M. K. (1991). Numerical solution of the Navier-Stokes equations using a finite element method, International Journal for Numerical Methods in Fluids, Vol. 13, pp. 481-489

Mehta, R. C. (2001). Comparative study of surface pressure fluctuations over bulbous heat shield at Mach 0.95, Computers & Fluids, Vol. 30, No. 6, pp. 689-709

Mehta, R. C. (2011). Block Structured Finite Element Grid Generation Method, paper accepted for publication in Computational Fluid Dynamics Journal

Mehta, R. C. (2006).Aerodynamic Drag Coefficient for Various Reentry Configurations at High Speed, AIAA paper 2006-3179

Mehta, R. C. (2004). Computation of flow field over reentry capsules at supersonic Mach numbers, Computational Fluid Dynamics JOURNAL, Vol. 13, No. 3, pp. 585-596

Mehta, R. C. (2008). Computations of flow field over Apollo and OREX reentry modules at high speed, Indian Journal of Engineering and Materials Sciences, Vol. 15, pp. 459-466

Mehta, R. C. (2010). Flow field simulations over reentry modules at high speed, Journal of Aerospace Sciences and Technologies, Vol. 62 , No. 1, pp. 55-65

Mehta, R. C. (2007). Three-dimensional inviscid flow field computation over various reentry configurations, AIAA paper 2007-133

Mehta, R. C. and Tiwari, S. B. (2008). Comparative studies of aerodynamic drag using inviscid flow computation and Newtonian method at high speed, Journal of Aerospace Sciences and Technologies, Vol. 60, No. 1, pp. 35-44

Moretti, G. (1979). Conformal mapping for the computation of steady three-dimensional supersonic flows, Numerical/Laboratory for Computer Methods in Fluid Mechanics , edis.- A. A. Pouring and V. I. Shah, ASME New York, pp. 13-28

Osu, H., Abe, T., Ohnishi, Y. Sasoh, A. and Takayama, K., (2002).Numerical investigation of high enthalpy flow generated by expansion tube, AIAA Journal, Vol. 40, No. 12, pp. 2423-2430

Otten, H. B. A. (2001). Preliminary computational investigation on aerodynamic phenomena DELFT aerospace reentry test vehicle, , in the proceedings of the 4th European Symposium on Aerothermodynamics for Space Applications, ESA, Capua, Italy, 15-18 October, pp. 207-213

Osher, S. (1984). Riemann solvers, the entropy condition and difference approximations, SIAM Journal of Numerical Analysis, Vol. 21, 1984, pp. 217-235

Osher, S., and Chakravarthy (1984). S. R., High resolution schemes and the entropy condition, SIAM Journal of Numerical Analysis, Vol. 21, pp. 955-984

Peyret, R., and Vivind, H. (1993). *Computational Methods for Fluid Flows,* Springer-Verlag, Berlin, pp. 109-111

Ritchtmyer, R. D., and Morton, K. W. (1967). *Difference Methods for Initial-Value Problems*, 2nd Edition, New York, Wiley, Interscience Publishers

Roe, P. L. (1981). Approximate Riemann solvers, parameter vectors and difference schemes, Journal of Computational Physics, Vol. 43, pp. 357-372

Roe, P. L. (1995). Upwind schemes using various formulations of the Euler equations in Numerical Methods for the Euler Equations of Fluid Dynamics, Philadelphia, PA, SIAM Publications

Rusanov, V. V. (1996). A blunt body in a supersonic stream, Annual Review of Fluid Mechanics, Vol. 8, pp. 377-404

Shang, J. S. (1984). Numerical Simulation of Wing-fuselage Aerodynamic Interference, AIAA Journal, Vol. 22, No. 10, pp. 1345-1353

Solazzo, M. A., Sansoner, A., Gasbarri, P. (1994). Aerodynamic characterization of the Carnia reentry module in the low supersonic regimes, in the proceedings of the 2nd European Symposium on Aerothermodynamics for Space Vehicles, ESTEC, Noordwiik, The Netherlkands, 21-25 November, pp. 41-47

Srinivasan, S. and Weilmuenster, K. J. (1987). Simplified curve fits for the thermodynamic properties of equilibrium air, NASA TP 1181

Steger, J. L., and Warming, R. F. (1981). Flux vector splitting of the inviscid gas dynamics equations with applications to finite difference methods, Journal of Computational Physics, Vol. 40, pp. 263-293

Tam, L. T. (1992). LU-SGS implicit scheme for entry vehicle flow computation and comparison with aerodynamic data, AIAA 92-2671 CP

Tai, C-S. and Kao, A. F. (1994). Navier-Stokes solver for hypersonic flow over a slender cone, Journal of Spacecraft and Rockets, Vol. 31, No. 1, pp. 215-222

Teramoto, S., Hiraki, K., Fujii, K. (2001). Numerical analysis of dynamic stability of a reentry capsule at transonic speeds, AIAA Journal, Vol. 39, No. 4, pp. 646-653

Teramoto, S., and Fujii, K. (2002) Mechanism of dynamic instability of a reentry capsule at transonic speeds, AIAA Journal, Vol. 40, No. 12, pp. 2467-2476

Truit, R. W. (1959). *Hypersonic Aerodynamics,* The Ronald Press Co., New York

Venkatapathy, E., Palmer, G., and Prabhu, D. K. (1991). AFE base computations, AIAA paper 91-1372

Van Leer, B., (1979). Towards the ultimate conservative difference scheme, V A second orders equal to Godunov's method, Journal of Computational Physics, Vol. 32, pp. 101-136

Walpot, I. (2001). Numerical analysis of the ARD capsule in S4 wind tunnel, in the proceedings of the 4th European Symposium on Aerothermodynamics for Space Applications, ESA, Capua, Italy, 15-18 October, pp. 523-527

Weinbaum, S. (1966). Rapid expansion of a supersonic boundary layer and its applications to the near wake, AIAA Journal, Vol. 4, No. 2, pp. 217-226

White, F. M. (1991). *Viscous Fluid Flow*, 2nd Edition, McGraw Hill International Edition, Singapore

Wood, W. A., Gnoffo, P. A., and Rault, D. F. G. (1996). Aerothermodynamic analysis of commercial experiment transporter (COMET) reentry capsule, AIAA paper 96-0316

Wood, A. W., Gnoffo, P. A. and Rault, D.F.G. (1996). Aerodynamic analysis of commercial experiment transport reentry capsule, Journal of Spacecraft & Rockets, Vol. 33, No. 5, 1996, pp. 643-646

Wood, W. A. (1997). Hypersonic pitching-moment shift for star dust reentry capsule fore body, NASA TM 97-206266

Wright, J. M., Milos, F. S., and Tran, P. (2006), Afterbody aero-heating flight data for planetary probe thermal protection system design, Journal of Spacecraft and Rockets, Vol. 43, No. 5, pp. 929-943

Yamamoto, Y. and Yoshioka, M. (1995). CFD and FEM coupling analysis of OREX aero-thermodynamic flight data, AIAA 95-2087

Yee, H. C. (1985). On symmetric and upwind TVD schemes, Proceedings of the 6th GAMM Conference on Numerical Methods in Fluid Mechanics, Braunschweig, Vieweg, pp. 399-407

Computational Simulations and Applications

Edited by Dr. Jianping Zhu

ISBN 978-953-307-430-6
Hard cover, 560 pages
Publisher InTech
Published online 26, October, 2011
Published in print edition October, 2011

The purpose of this book is to introduce researchers and graduate students to a broad range of applications of computational simulations, with a particular emphasis on those involving computational fluid dynamics (CFD) simulations. The book is divided into three parts: Part I covers some basic research topics and development in numerical algorithms for CFD simulations, including Reynolds stress transport modeling, central difference schemes for convection-diffusion equations, and flow simulations involving simple geometries such as a flat plate or a vertical channel. Part II covers a variety of important applications in which CFD simulations play a crucial role, including combustion process and automobile engine design, fluid heat exchange, airborne contaminant dispersion over buildings and atmospheric flow around a re-entry capsule, gas-solid two phase flow in long pipes, free surface flow around a ship hull, and hydrodynamic analysis of electrochemical cells. Part III covers applications of non-CFD based computational simulations, including atmospheric optical communications, climate system simulations, porous media flow, combustion, solidification, and sound field simulations for optimal acoustic effects.

InTech Europe
University Campus STeP Ri
Slavka Krautzeka 83/A
51000 Rijeka, Croatia
Phone: +385 (51) 770 447
Fax: +385 (51) 686 166
www.intechopen.com

InTech China
Unit 405, Office Block, Hotel Equatorial Shanghai
No.65, Yan An Road (West), Shanghai, 200040, China
中国上海市延安西路65号上海国际贵都大饭店办公楼405单元
Phone: +86-21-62489820
Fax: +86-21-62489821